A van der Waals Heterostructure with an Electronically Textured Moiré Pattern: $PtSe_2/PtTe_2$

Li, J.; Ghorbani Asl, M.; Lasek, K.; Pathirage, V.; Krasheninnikov, A.; Batzill, M.;

Originally published:

March 2023

ACS Nano 17(2023)6, 5913-5920

DOI: https://doi.org/10.1021/acsnano.2c12879

A van der Waals Heterostructure with an Electronically Textured Moiré Pattern: $PtSe_2/PtTe_2$

Jingfeng Li,[1] Mahdi Ghorbani-Asl,[2] Kinga Lasek,[1] Vimukthi Pathirage,[1] Arkady V. Krasheninnikov,[2,3] Matthias Batzill[1,*]

[1] Department of Physics, University of South Florida, Tampa, FL 33620, USA
[2] Helmholtz-Zentrum Dresden-Rossendorf, Institute of Ion Beam Physics and Materials Research, 01328 Dresden, Germany
[3] Department of Applied Physics, Aalto University, P.O. Box 11100, 00076 Aalto, Finland

* Corresponding author: Matthias Batzill; e-mail: mbatzill@usf.edu

Abstract:

The interlayer interaction in Pt-dichalcogenides strongly affects their electronic structures. The modulations of the interlayer atom-coordination in vertical heterostructures based on these materials are expected to laterally modify these interlayer interactions and thus provide an opportunity to texture the electronic structure. To determine the effects of local variation of the interlayer atom coordination on the electronic structure of $PtSe_2$, van der Waals heterostructures of $PtSe_2$ and $PtTe_2$ have been synthesized by molecular beam epitaxy. The heterostructure forms a coincidence lattice with 13-unit cells of $PtSe_2$ matching 12-unit cells of $PtTe_2$, forming a moiré superstructure. The interaction with $PtTe_2$ reduces the band gap of $PtSe_2$ monolayers from 1.8 to 0.5 eV. While the band gap is uniform across the moiré unit cell, STS and dI/dV mapping identify gap states that are localized within certain regions of the moiré unit cell. Deep states associated with chalcogen p_z-orbitals at binding energies of ~-2 eV also exhibit lateral variation within the moiré unit cell, indicative of varying interlayer chalcogen interactions. Density functional theory calculations indicate that local variations in atom coordination in the moiré unit cell causes variations in the charge transfer from $PtTe_2$ to $PtSe_2$ thus affecting the value of the interface dipole. Experimentally this is confirmed by measuring the local work function by field emission resonance spectroscopy, which reveals a large work function modulation of ~0.5 eV within the moiré structure. These results show that the local coordination variation of the chalcogen atoms in the $PtSe_2/PtTe_2$ van der Waals heterostructure induces a nanoscale electronic structure texture in $PtSe_2$.

TOC figure:

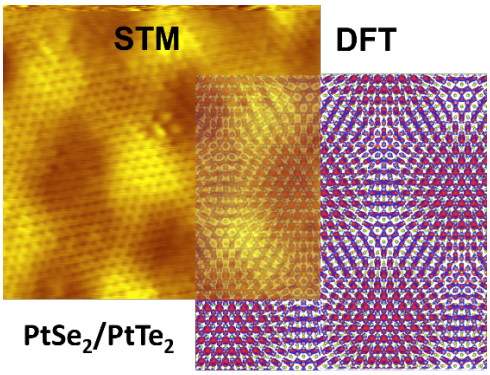

One of the most exciting features of van der Waals (vdW) heterostructures is the formation of moiré structures due to long-range coincidence lattices formed by the combination of materials with different lattice constants or rotation (twist) angles. Despite weak interlayer interactions, different relative atom positions within the moiré unit cell cause a periodic potential that modifies the electronic structure of the two-dimensional (2D) materials. These moiré patterns in vdW- heterostructures thus allow an additional degree of engineering of materials properties, which has been utilized to demonstrate new phenomena and potential applications. Some of the properties that have emerged due to moiré super-periodicities in vdW heterostructures are: (i) the lateral moiré superstructure gives rise to superlattice Dirac points and consequently Hofstadter butterfly states. This has been observed in h-BN/graphene vdW-heterostructures.[1,2] (ii) Moiré structures formed by twisting two graphene lattices result in strongly correlated Mott insulator or superconducting states at precisely controlled twist angles,[3,4,5] and (iii) in semiconducting transition metal dichalcogenide (TMD) heterostructures interlayer interactions induce local modulations of their band gaps[6,7] that may cause flat bands,[8,9] quantized confined states,[10] and optical excitations of the so-called moiré excitons.[11,12] Here we explore another periodic texturing in the electronic properties induced by moiré superlattice in vdW heterostructures in the form of lateral work function modulations. To accomplish strong work function modulations in the moiré structures, the interlayer charge redistribution must depend on local interlayer atom coordination within the moiré unit cell. This has been shown for monolayer materials deposited on crystalline supports such as NaCl-,[13] FeO-,[14,15] or Pb[16]- monolayers on silver, platinum, or silicon crystals, respectively. More prominently this effect has been also explored for graphene on Rh[17] or h-BN on various transition metals (e.g. Rh,[18] Ru,[19] Cu,[20,21] Ir,[22]) where the varying coordination of the BN atoms with respect to the surface metals gives rise to strongly variable chemical interactions causing large corrugation of the h-BN layer and consequently modulations of interlayer dipoles and local work function.[23] Subsequently, it was also shown that the work function modulation of such a hex-BN monolayer on a metal substrate can be transferred further to a semiconducting $MoSe_2$ layer epitaxially grown on the hex-BN/metal substrate.[24] In this study we are aiming to establish such electronic modulations in a pure, potentially free-standing vdW system, *i.e.*, averting a 3D-metal substrate. In order to achieve the strongly modulated interlayer interactions that can cause the desired work function modulations, we explore the platinum dichalcogenide system, which has demonstrated extraordinary layer-dependencies of their electronic structure.[25,26,27,28,29] $PtSe_2$ and $PtTe_2$ exhibit a band gap of 1.8 eV and 0.5 eV, respectively, as monolayers,[30] but become semi-metals for multilayer samples indicating the strong dependence of their electronic structure on interlayer interactions. This dependence on interlayer interaction makes them promising materials for studying effects of moiré structures on the electronic properties in vdW heterostructures. Moreover, the work function variation within a moiré unit cell is more pronounced for larger unit cells,[21] which can be achieved by appropriate differences in the lattice constants. The larger lattice constants of tellurides versus selenides of the same transition metal makes their combination into heterostructures ideal for creating such moiré patterns. Here we show that the electronic structure of $PtSe_2$ monolayer grown on $PtTe_2$ is modulated by the varying interlayer interaction in the moiré pattern and the work function in $PtSe_2/PtTe_2$ heterostructure is indeed strongly modulated by close to 0.5 eV within the moiré unit cell. Thus, this demonstrates an electronically textured moiré-pattern in a pure vdW-heterostructure system.

Results and Discussion

$PtSe_2$ monolayers are synthesized on $PtTe_2$ ultrathin films by molecular beam epitaxy (MBE). Fig. 1 (a) shows a large-scale STM image of a few layer $PtTe_2$ film grown on a HOPG substrate. $PtTe_2$ films on HOPG

exhibits large flat terraces with only terrace steps of ~0.4 nm height, corresponding to the interlayer separation between $PtTe_2$ van der Waals layers. This film is used as a substrate for $PtSe_2$ growth. Interestingly, $PtSe_2$ grows in a Stranski-Krastanov-like growth mode, with the first monolayer wetting the surface and subsequent growth resulting in cluster formation, see supplemental information Fig. S1. While such a growth for 2D materials is unusual and its mechanism not well understood for this system, it facilitates the study of monolayer $PtSe_2$ on $PtTe_2$ films. Fig. 1(b) shows the deposition of close to one monolayer of $PtSe_2$ on the $PtTe_2$ substrate. The surface exhibits the same atomic height steps as for pure $PtTe_2$, suggesting that the step-structure of the underlying $PtTe_2$ substrate is not affected by the $PtSe_2$ growth. The surface now exhibits a moiré pattern whose periodic modulation is observed in the STM images. Figure 1(c) shows a high-resolution STM image of the moiré structure and its Fourier transformation with the corresponding Fourier-filtered images. From Fig. 1(c) the moiré unit cell is determined to consist of 13 $PtSe_2$ unit cells, which is consistent with a close coincidence lattice of $13 \times a_{PtSe2}$ (13×0.38 nm = 4.94 nm) on $12 \times a_{PtTe2}$ (12×0.41 nm = 4.92 nm). In addition to this majority moiré structure formed by van der Waals heterostructure of rotationally aligned $PtSe_2$ and $PtTe_2$ lattices, a slightly rotated structure is also observed. These two moiré structures are rotated by ~ 11° relative to each other as shown in Fig. 1(d). The rotation angles of the moiré unit cells are amplifying small rotations of the atomic lattices and an 11° rotation of the moiré unit cells corresponds to only a ~1° rotation of the atomic lattices (see Fig. S2) so that the grown $PtSe_2$ monolayer is still roughly aligned with the $PtTe_2$ substrate. The amplification of the rotation of the moiré structure also enables to identify the aligned from the rotated $PtSe_2$ monolayer. If the $PtSe_2$ monolayer is aligned with the $PtTe_2$ substrate the atomic unit cell of $PtSe_2$ is also aligned with the moiré unit cell, while if the $PtSe_2$ layer is rotated by ~1˚ relative to the $PtTe_2$ substrate than the moiré unit cell is rotated by ~10˚ relative to the $PtSe_2$ unit cell, which can be observed in atomic resolution images. Generally, the order and long-range coherence of the moiré structure in this $PtSe_2/PtTe_2$ system is less than in many of the related moiré patterns of monolayer films on metal supports discussed above. One possible reason is the lower synthesis temperature for this system, which is limited to ~ 300 ˚C. At higher growth temperatures an intermixing of the $PtSe_2$ with the $PtTe_2$ substrate is observed. The relatively low thermal stability of these phases has also been reported for pure $PtTe_2$ which results in easy loss of Te and transformation into different compositional phases upon vacuum annealing.[31]

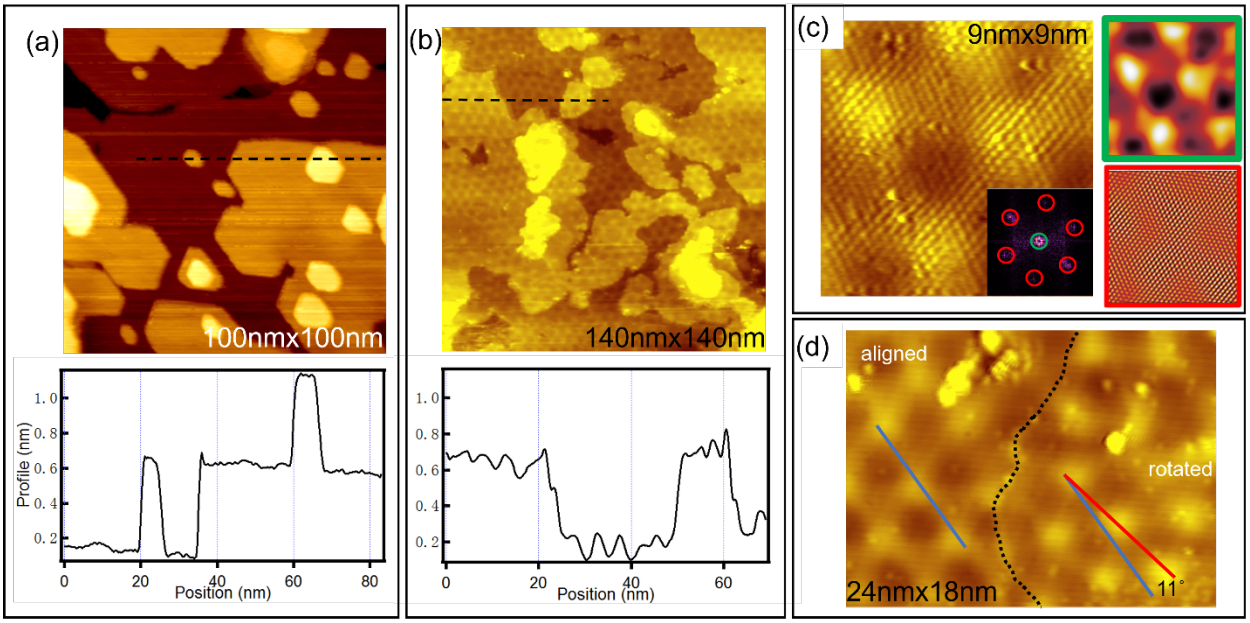

Fig. 1: STM characterization of the morphology of $PtSe_2/PtTe_2$ heterostructure. (a) $PtTe_2$ multilayers on HOPG, which serves as the substrate for $PtSe_2$ growth. The line profile along the dashed line is shown in the bottom panel and shows step heights corresponding to the interlayer separation of $PtTe_2$. (b) STM image of monolayer $PtSe_2$ on $PtTe_2$. The surface is uniformly covered with a moiré structure and the step heights correspond to that of the underlying $PtTe_2$ substrate. The black dashed lines indicate the location of the line profiles shown in the bottom panel. Tunneling condition V_{bias}=3V, I_t=0.2nA. (c) High-resolution STM image of the moiré structure and its Fourier transformations (a larger version of the Fourier transformation can be found in Fig. S3). The red and green circles in the Fourier transformation indicate the atomic- and moiré - periodicity, respectively, and the corresponding Fourier-filtered images are shown. Tunneling condition V_{bias}=0.5V, I_t=0.1nA. (d) Two observed moiré structures, separated by the dashed line. These two moiré structures originate from a small rotation of the $PtSe_2$ lattice with respect to the $PtTe_2$ substrate. The red and blue lines indicate the direction of the moiré unit cell, which illustrate the roughly 11˚ rotation between these two moiré unit cell directions. Tunneling condition V_{bias}=3V, I_t=0.2nA.

Interface states: $PtSe_2$ exhibits strong layer-dependent electronic properties. STS measurements for mono-, bi-, and tri-layer $PtSe_2$ exhibit band gaps of 1.8 eV, 0.6 eV, and 0 eV, respectively, as shown in Fig. 2(a) for $PtSe_2$ layers grown directly on the HOPG substrate. These extraordinarily strong variations are due to interlayer interactions in the Pt-dichalcogenide family. This raises the question of how the interlayer interactions between a $PtSe_2$ on a $PtTe_2$ substrate affect the electronic structure of a monolayer $PtSe_2$. The interlayer interactions are dominated by the frontier *p*-orbitals of the chalcogen atoms, whose overlap in the vdW gap gives rise to the closing of the band gaps in the pure materials. In the heterostructure interlayer interactions may be dominated by the *4p*- and *3p*- orbitals of Te- and Se- atoms, respectively. Thus, the interaction between the different chalcogen atoms and their spatially varying coordination within the moiré structure is anticipated to contribute to local electronic structure variation within the moiré unit cell. STS measurements of the electronic structure of monolayer $PtSe_2$ on $PtTe_2$ in different regions of the moiré unit cell are shown in Fig. 2(b). We consider three high symmetry sites of the moiré structure as follow: (i) $PtSe_2$ is in registry with $PtTe_2$, *i.e.*, the two structures form a 1T-stacking, and therefore denoted '1T-site', (ii) sites where Se-atoms are on top of Te-atoms, denoted as 'Se-Te site', and (iii) Se atoms are over the Pt-sites in the $PtTe_2$ layer, and thus denoted 'Se-Pt site'. These three sites

are illustrated in Fig. 2(e). It can be seen that similar to bi-layer $PtSe_2$, the band gap in monolayer $PtSe_2$ on $PtTe_2$ is also narrowed as compared to quasi-freestanding $PtSe_2$ monolayers grown on a HOPG substrate, but a band gap, similar to that observed for bilayer $PtSe_2$, of ~ 0.5 eV remains. This indicates that the interlayer interactions between $PtSe_2$ and $PtTe_2$ have a similar effect on the gap as in $PtSe_2$-$PtSe_2$ contacts. While the band gap narrowing of monolayer $PtSe_2$ on $PtTe_2$, compared to free-standing monolayer $PtSe_2$, is uniform across the moiré unit cell, there are variations in the local density of states (LDOS) within different regions of the moiré unit cell. Electronic states can be identified with a strong variation at -0.8 eV below the Fermi level, as reflected in the dI/dV map. These states at -0.8 eV binding energy are most pronounced at site (i) and absent at site (iii). We demonstrate its localization by comparing the topographic STM image with dI/dV mapping shown in Fig. 2(c) and (d), respectively. Comparison of the aligned with that of the slightly rotated $PtSe_2$ moiré structure shows that the states at -0.8eV show an even stronger localization at site (ii) in the moiré unit cell (see Fig. S5).

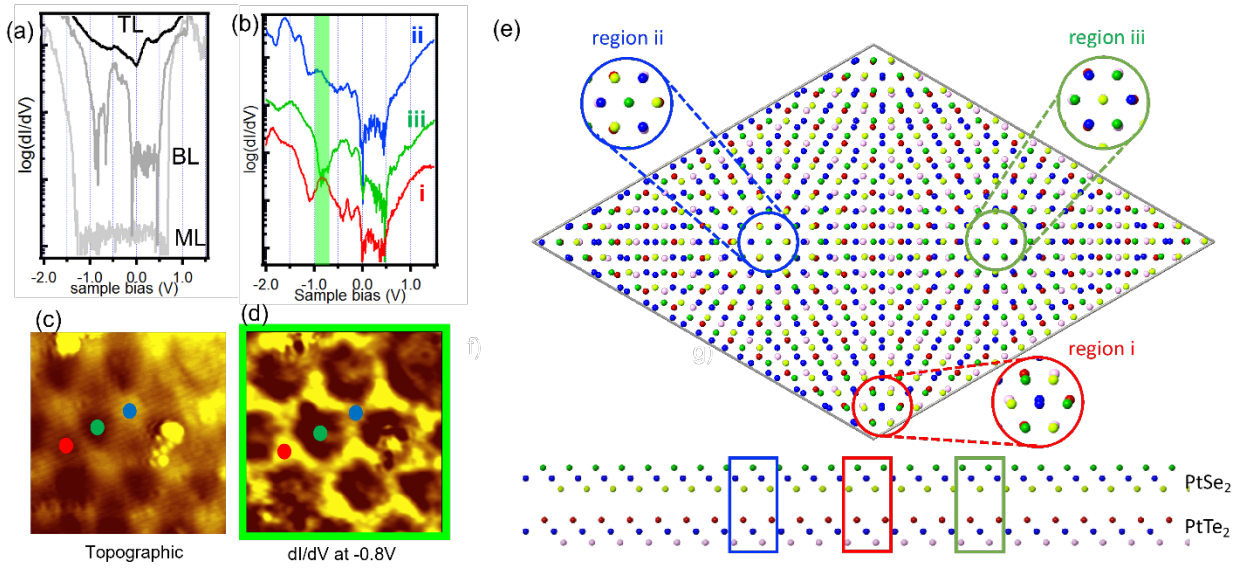

Fig. 2: Electronic structure of $PtSe_2$. (a) Shows layer dependence of the dI/dV spectra of $PtSe_2$ grown on a HOPG substrate. STM images of $PtSe_2$ islands and location of the STS spectra is shown in Fig. S4. The monolayer (ML) exhibits a large band gap of 1.8 eV, the bilayer (BL) has a band gap of 0.6 eV, and the trilayer (TL) is metallic. (b) Selected dI/dV spectra of $PtSe_2$-monolayer on $PtTe_2$ substrate at high symmetry sites of the moiré structure (set point for STS: I=100pA, V=0.6V). The dI/dV spectra are plotted on a log-scale, the same spectra in (a) and (b) can be found plotted on a linear scale in Fig. S6. The position at which the color-coded spectra were taken is also indicated in the STM image shown in (c). A dI/dV map taken at -0.8 eV of the same region is shown in (d), highlighting the localized distribution of the electronic state at -0.8 eV. The atomic structure model of the moiré unit cell is presented in (e), a detailed description of the three low symmetry sites can be found in the text.

Electronic states within an energy window for which the free standing $PtSe_2$ monolayer exhibits a band gap can be attributed to originating from the interlayer interaction with the $PtTe_2$ substrate. In addition to these 'shallow' states, we also observe lateral modulations of electronic states further away from the Fermi-level. These deep states are shown in Fig. 3 for a region that shows both moiré structures due to a $PtSe_2$ domain that is aligned with $PtTe_2$ and a domain with a slight rotation of the $PtSe_2$ layer with respect to $PtTe_2$. Electronic states at -1.6 eV and -2 eV are clearly discerned in the dI/dV spectroscopy. Based on

previous calculations, these states are associated with $p_{x,y}$ and p_z chalcogen orbitals, respectively.[32] Modulations of these states are observed for both moiré structures but are more pronounced in the domains where the $PtSe_2$ is rotated with respect to the $PtTe_2$. The p_z state at -2 eV is observed in regions i and iii of the aligned moiré but is suppressed in region ii. This suggests that the states associated with p_z orbitals are altered if the chalcogen atoms in the two layers are on top of each other. In contrast, the states at -1.6 eV are associated with p_{xy} orbitals and those are less affected in the moiré structure. Interestingly the p_z states have been associated with a spin texture of $PtSe_2$ monolayers[32] and thus their modulation in the moiré structure implies a local modulation also of this spin texture.

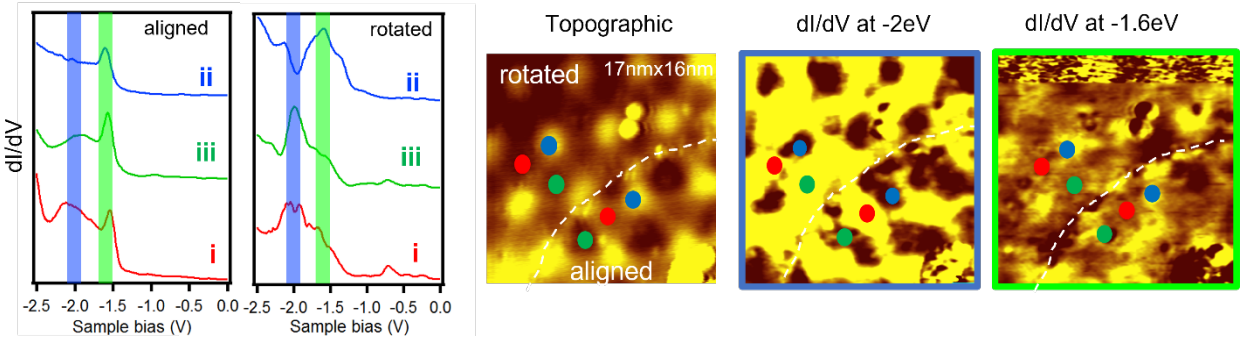

Fig. 3: dI/dV spectroscopy of deep states for different positions in the two moiré structures (set point for STS: I=100pA, 1V). For modulations of shallow states in the rotated domains, detailed spectra are shown in Fig. S5. Two main states can be identified at -1.6 eV and -2 eV, which may be attributed to $p_{x,y}$ and p_z derived selenium states, respectively. The STM image (tunneling condition: V_{bias}=3V, I_t=0.2nA) shows both aligned and rotated moiré domains. The domain boundary is indicated by the dashed line. The state at -2eV exhibits a stronger localization within regions i and iii, while it is absent in region ii. The state at -1.6 eV is less modulated within the moiré structure, supporting the assignment to $p_{x,y}$ derived states.

Work function: Determining work function variations in nanoscale structures by field emission resonance (FER) spectroscopy has been widely used in scanning tunneling microscopy .[13,14,15,16,17,18,19,20,21,22,23,24,33,34,35] Briefly, in FER the bias voltage between an STM tip and the sample surface is chosen such that the Fermi level of the STM tip lies above the vacuum level of the sample. In this Fowler-Nordheim tunneling regime, the drop of the potential in the tunnel junction causes a potential well between the tip and the sample surface. The quantum confined image potential states in this quantum well are probed in FER spectroscopy. Local changes in the substrate work function modify the image potential states and thus a shift of the resonance states is a direct measure of the work function modulations along the surface. It is generally challenging to determine absolute values of the work function because the STM tip properties are not well-defined, but for a stable tip the relative changes for different substrate sites are given by the shift of the resonance states.

Figure 4 shows FERs at different positions along a line across the moiré unit cell. All FERs, apart from the lowest energy one, which is known to be unreliable,[20,23,24,**Error! Bookmark not defined.**] shift approximately by the same amount. Reported evidence suggests that the second FER is the most relevant for measuring work function variations,[**Error! Bookmark not defined.**,36] and therefore the reported values refer to that of the 2nd FER. The largest work function is observed for site ii which is 0.48 eV larger than for site iii. Site i is in between, with a work function 0.28 eV lower than site ii. Slightly less work function modulations are observed for the rotated moiré structure as shown in Fig. S7. This is a substantial work function difference and the first

reported for a transition metal dichalcogenide vdW heterostructure. Strong modulations of the work function imply surface dipoles that must originate from interlayer charge transfer in the $PtSe_2/PtTe_2$ heterostructure. To gain further insight in the experimentally observed work function modulations, density functional theory (DFT) calculation of the local electronic structure and charge transfer within the moiré structure have been performed, which is discussed next.

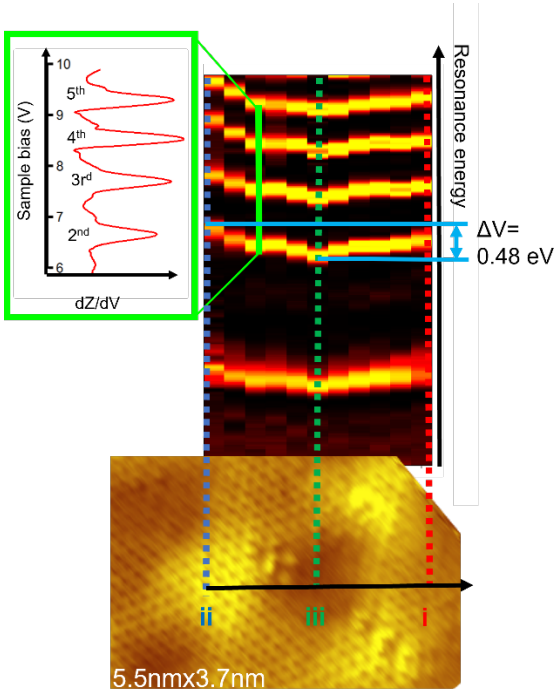

Fig. 4: Work function modulation within moiré unit cell measured by field emission resonance (FER) spectroscopy. FER spectra are measured along the moiré unit cell from regions ii-to-iii-to-i. One spectrum is shown as an example and the others are plotted as an intensity map to illustrate the variation of the resonances as a function of the position. The largest resonance energy difference is observed between regions ii and iii and is measured to be 0.48 eV. The strong variations of the FER at different sites of the moiré unit cell demonstrate the work function modulation within the moiré unit cell. The imaging conditions for the STM data are: V_{bias}=0.5V, I_t=0.1nA.

$PtSe_2/PtTe_2$ moiré structure and electronic properties from DFT calculations: To obtain deeper insights into the atomic structure of the interface, we performed extensive DFT calculations using an unsupported $PtSe_2/PtTe_2$ supercell as a model heterostructure, see the Methods section for detail. A supercell with a single $PtTe_2$ layer, rather than multilayers as in the experiments, is necessitated by the computational limitations imposed by the large number of heavy atoms in the structure. Test simulations on a smaller unit cell with rotated $PtSe_2/PtTe_2$ layers show that the band gap of monolayer $PtSe_2$ is not changed by the number of supporting $PtTe_2$ layers (Fig. S8). This illustrates that the monolayer $PtTe_2$ can be a reasonable model system to qualitatively describe the behavior in the experimental system. The computed relaxed crystal structure exhibits only very weak topographical buckling of the bilayer structure, implying that the observed apparent topography in STM images is likely associated with an electronic contrast, however, this needs to be verified by structural probes.

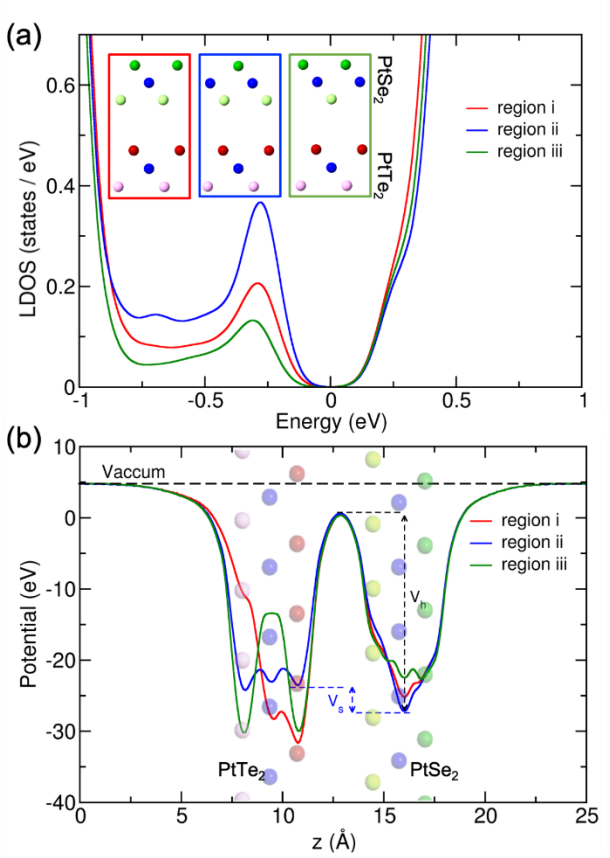

Fig. 5: (a) Local density of states for different regions in the moiré structures of the $PtSe_2$/$PtTe_2$ heterostructure. The LDOS is shown for $PtSe_2$. (b) Electrostatic potential along the direction perpendicular to the heterostructure and averaged within planes parallel to the heterostructure.

Depending on the relative positions of the interface Se atoms in the $PtSe_2$ with respect to the interface Te atoms in the $PtTe_2$ monolayer, see Figure 2 (e), the Se-Te interatomic distances and angles are different in different regions of the moiré pattern. As a result, the local interactions between the layers is different giving rise to the variation of the local electronic structure. Figure 5 (a) shows LDOS at three moiré sites in the heterostructure. The calculated band gap edge energies of the $PtSe_2$/$PtTe_2$ heterostructure are almost unchanged for the different sites within the moiré structure with only small variations of less than 30 meV (see Fig. S9), and thus the 'local' band gap remains nearly constant within the moiré unit cell (note that the calculated band gap energy depends sensitively on inclusion of spin-orbit coupling in the calculations, see Table S1), the LDOS below the Fermi level (at about -0.3 eV) is larger in region ii, as compared to the other sites. The constant band gap is consistent with the experimental STS data. Also, the variation of the LDOS at the band edge is consistent with the STM apparent topographic appearance (see Fig. 2(c)) of the heterostructure indicating higher tunneling contrast in region ii than in the other two moiré regions. We further analyzed the modulation of the averaged electrostatic profile perpendicular to the heterostructure at different sites in the moiré structure, Figure 5 (b), where the differences are evident. The variation of the electrostatic potential at different sites is caused by the amount of charge transfer at the specific interface area. Our results indicate that the potential height V_h at the $PtSe_2$ layer is larger in region ii than in the other two regions. This is consistent with the calculated Bader charges

transferred from $PtTe_2$ to $PtSe_2$, which were found to be 4×10^{-3}, 7×10^{-3} and 2×10^{-3} electrons/atoms for regions i, ii and iii, respectively, see Figure 6. The charge transfer from $PtTe_2$ to $PtSe_2$ is related to the difference in the work functions, which can be described by the relation $Q \propto \Delta\varphi$, where Q represents the charge, and $\Delta\varphi$ is the difference in the work functions between the two monolayers, respectively.[37] These charge transfers can be associated with the experimentally measured work function modulations. Since the native $PtSe_2$ bilayer does not exhibit such work function modulations, such behavior in the heterostructure can be attributed solely to charge transfer-induced dipoles at the $PtSe_2/PtTe_2$ interface.

(a)

region	Δq_{PtSe2}
region i	4×10^{-3} e/atom
region ii	7×10^{-3} e/atom
region iii	2×10^{-3} e/atom

$\Delta q_{PtSe2} = q_{PtSe2}$(heterostructure) - q_{PtSe2} (monolayer)

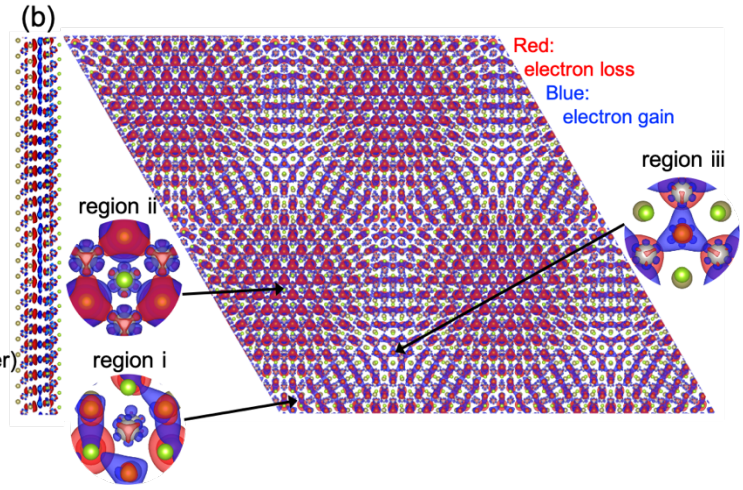

Fig. 6: (a) Average Bader charges at each region in the $PtSe_2/PtTe_2$ heterostructure with $PtSe_2$ being on top, as compared to the isolated $PtSe_2$ monolayer. (b) The charge transfer between $PtSe_2$ and $PtTe_2$ layers calculated as a difference between the charge in the heterostructure and the isolated monolayers. Blue and red represent charge accumulation and charge depletion. Note the variation of charge in different areas of the moiré pattern.

Conclusion

In conclusion, we have shown that the $PtSe_2/PtTe_2$ vdW heterostructure is a strongly electronically corrugated moiré system, as evident from the experimental STM/STS data. Even with relatively weak interlayer interactions in a pure vdW bilayer the varying interlayer atom configuration within the moiré unit cell have pronounced effects on the local electronic structure. STS show that the atom coordination between the two materials causes interlayer states that vary within the moiré structure, and their localization is imaged by dI/dV mapping. The varying interactions of the chalcogen *p*-orbitals in the $PtSe_2/PtTe_2$ moiré unit cell are giving rise to varying interface dipoles and thus different local work functions. This has been experimentally determined by FER spectroscopy and work function shifts close to 0.5 eV have been observed for the different local stacking configurations. The strong local modulation of the work function implies in-plane dipoles to permit the electrostatic potential offsets. Surface dipoles and work function variations have been shown to facilitate the alignment of molecular adsorbates on hex-BN/metal substrates,[38,39,40,41,42] and the control over the adsorbate charge transfer within the moiré structure,[43,44] and similar effects can be anticipated for this purely vdW heterostructure. Pt-

dichalcogenides have also shown promise for hydrogen evolution and oxygen reduction electrocatalysis.[45,46,47] Work function engineering by the formation of vdW heterostructures is an approach to tune their surface chemical properties, and thus vdW heterostructures may be anticipated to exhibit varying and intriguing electrocatalytic properties as compared to their individual components. Moreover, the Pt-chalcogenides are known for their spin textures[32,48] and magnetic properties[49,50] and the interaction of the local spins with the periodic moiré -dipoles may give rise to magnetic properties modulations within the moiré structure. Moreover, STS studies have detected variation of p_z-orbitals, which have been associated with spin texture in Pt-dichalcogenides.[32] This may indicate a lateral modulation of such spin textures within the moiré unit cell. Local magnetic properties may be studied by spin-resolved STS in the future.

Methods

Experimental: $PtTe_2$ and $PtSe_2$ are grown in dedicated tellurium and selenium growth chambers by co-deposition of Pt and chalcogens. First a $PtTe_2$ multilayer film is grown at 300 ˚C substrate temperature on a freshly cleaved and vacuum-annealed HOPG substrate.[31,51] Subsequently, a monolayer of $PtSe_2$ is grown on top of the $PtTe_2$ at growth temperature of 300 ˚C. For both compounds, Pt was evaporated in an e-beam evaporator from a 2mm solid Pt-rod. Tellurium was supplied from a Knudsen cell and selenium from a hot-wall valved cracker source. In either case, the chalcogen to Pt-flux ratio exceeded a 10:1 ratio. The prepared films were characterized in a closed-cycle low-temperature STM with a base temperature close to 20 K. The bias voltage was applied to the sample, so the unoccupied and occupied states were recorded under positive and negative bias, respectively. dI/dV spectra were recorded with a lock-in amplifier with a 30 mV modulation voltage and the feedback-loop turned off. The FER spectra were obtained from recording Z-V, with the feedback-loop on, as a function of applied bias voltage and dZ/dV was obtained by calculating the derivative numerically.

Computational: Density functional theory (DFT) calculations were performed using Vienna Ab initio Simulation Package, within the plane-wave projector augmented-wave (PAW) method.[52,53] The exchange-correlation functional was employed in the generalized gradient approximation of Perdew-Burke-Ernzerhof.[54] An energy cutoff of 400 eV was set for plane-wave expansion of the supercell calculations. van der Waals interactions were taken into account using the many-body dispersion combined with fractional ionic atoms method.[55] The effect of spin-orbit coupling is included in the electronic structure calculations. The Brillouin zone of the supercells was sampled using Gamma-point approximation. The charge densities were illustrated using the VESTA package.[56] The $PtSe_2$/$PtTe_2$ heterostructure was constructed by using an interface consisting of 13 × 13 unit cells of $PtSe_2$ and 12 × 12 unit cells of $PtTe_2$ monolayer corresponding to a lattice mismatch of only 0.9%. The supercell has a lattice constant of a=b=48.65 $\AA$ including 939 atoms.

Acknowledgement: Financial support from the National Science Foundation under award 2140038 is acknowledged. A.V.K. thanks the German Research Foundation (DFG) for the support through Project KR 4866/6-1 and the collaborative research center “Chemistry of Synthetic 2D Materials” SFB-1415-417590517. The authors further thank the HZDR Computing Center, HLRS, Stuttgart, Germany, and TU Dresden Cluster “Taurus” for generous grants of CPU time.

[1] Dean, C. R.; Wang, L.; Maher, P.; Forsythe, C.; Ghahari, F.; Gao, Y.; Katoch, J.; Ishigami, M.; Moon, P.; Koshino, M.; Taniguchi, T.; Watanabe, K.; Shepard, K.L.; Hone, J.; Kim, P. Hofstadter's Butterfly and the Fractal Quantum Hall Effect in Moiré Superlattices. *Nature* **2013**, *497*, 598–602.

[2] Hunt, B.; Sanchez-Yamagishi, J. D.; Young, A. F.; Yankowitz, M.; LeRoy, B. J.; Watanabe, K.; Taniguchi, T.; Moon, P.; Koshino, M.; Jarillo-Herrero, P.; Ashoori, R. C. Massive Dirac Fermions and Hofstadter Butterfly in a van der Waals Heterostructure. *Science* **2013**, *340*, 1427-1430.

[3] Cao, Y.; Fatemi, V.; Demir, A.; Fang, S.; Tomarken, S.L.; Luo, J.Y.; Sanchez-Yamagishi, J.D.; Watanabe, K.; Taniguchi, T.; Kaxiras, E.; Ashoori, R.C.; Jarillo-Herrero, P. Correlated Insulator Behaviour at Half-Filling in Magic-Angle Graphene Superlattices. *Nature* **2018**, *556*, 80-84.

[4] Cao, Y., Fatemi, V.; Fang, S.; Watanabe, K.; Taniguchi, T.; Kaxiras, E.; Jarillo-Herrero, P. Unconventional Superconductivity in Magic-Angle Graphene Superlattices. *Nature* **2018**, *556*, 43-50.

[5] Cao, Y., Rodan-Legrain, D.; Rubies-Bigorda, O.; Park, J.M.; Watanabe, K.; Taniguchi, T.; Jarillo-Herrero, P. Tunable Correlated States and Spin-Polarized Phases in Twisted Bilayer–Bilayer Graphene. *Nature* **2020**, *583*, 215-220.

[6] Zhang, C.; Chuu, C.-P.; Ren, X.; Li, M.-Y.; Li. L.-J.; Jin. C.; Chou, M.-Y.; Shih. C.-K. Interlayer Couplings, Moiré Patterns, and 2D Electronic Superlattices in MoS_2/WSe_2 Hetero-Bilayers. *Sci. Adv.* **2017**, 3, e1601459.

[7] Susarla, S.; Sassi, L.M.; Zobelli, A.; Woo, S.Y.; Tizei, L.H.G.; Stéphan, O.; Ajayan, P.M. Mapping Modified Electronic Levels in the Moiré Patterns in MoS_2/WSe_2 Using Low-Loss EELS. *Nano Letters* **2021,** *21*, 4071-4077.

[8] Li, H.; Li, S.; Naik, M.H.; Xie, J.; Li, X.; Wang, J.; Regan, E.; Wang, D.; Zhao, W.; Zhao, S.; Kahn, S.; Yumigeta, K.; Blei, M.; Taniguchi, T.; Watanabe, K.; Tongay, S.; Zettl, A.; Louie, S.G.; Wang, F.; Crommie, M.F. Imaging Moiré Flat Bands in Three-Dimensional Reconstructed WSe_2/WS_2 Superlattices. *Nat. Mater.* **2021**, *20*, 945–950.

[9] Waters, D.; Nie, Y.; Lüpke, F.; Pan, Y.; Fölsch, S.; Lin, Y.-C.; Jariwala, B.; Zhang, K.; Wang, C.; Lv, H.; Cho, K.; Xiao, D.; Robinson, J.A.; Feenstra, R.M. Flat Bands and Mechanical Deformation Effects in the Moiré Superlattice of MoS_2-WSe_2 Heterobilayers. *ACS Nano* **2020**, *14*, 7564–7573

[10] Pan, Y.; Fölsch, S.; Nie, Y.; Waters, D.; Lin, Y.-C.; Jariwala, B.; Zhang, K.; Cho, K.; Robinson, J.A.; Feenstra, R.M. Quantum-Confined Electronic States Arising from the Moiré Pattern of MoS_2–WSe_2 Heterobilayers. *Nano Lett.* **2018**, *18*, 1849–1855.

[11] Regan, E.C.; Wang, D.; Paik, E.Y.; Zeng, Y.; Zhang, L.; Zhu, J.; MacDonald, A.H.; Deng, H.; Wang, F. Emerging Exciton Physics in Transition Metal Dichalcogenide Heterobilayers. *Nat. Rev. Mater.* **2022,** *7*, 778-795.

[12] Gogoi, P.K.; Lin, Y.-C.; Senga, R.; Komsa, H.-P.; Wong, S.L.; Chi, D.; Krasheninnikov, A.V.; Li, L.-J.; Breese, M.B.H.; Pennycook, S.J.; Wee, A.T.S.; Suenaga, K. Layer Rotation-Angle-Dependent Excitonic Absorption in van der Waals Heterostructures Revealed by Electron Energy Loss Spectroscopy. *ACS Nano* **2019**, *13*, 9541–9550.

[13] Pivetta, M.; Patthey, F.; Stengel, M.; Baldereschi, A.; Schneider, W.-D. Local work function Moiré pattern on ultrathin ionic films: NaCl on Ag(100). *Phys. Rev. B* **2005**, *72*, 115404.

[14] Rienks, E. D. L.; Nilius, N.; Rust, H.-P.; Freund, H.-J. Surface Potential of a Polar Oxide Film: FeO on Pt(111). *Phys. Rev. B* **2005**, *71*, 241404.

[15] Dahal, A.; Batzill, M. Growth from Behind: Intercalation-Growth of Two-Dimensional FeO Moiré Structure Underneath of Metal-Supported Graphene. *Sci. Rep.* **2015**, 5, 11378.

[16] Kim, H.; Hasegawa, Y. Spatial variation in local work function as an origin of moiré contrast in scanning tunneling microscopy images of Pb thin films/Si(111). *Japn. J. Appl. Phys.* **2016**, *55*, 08NA03.

[17] Wang, B.; Caffio, M.; Bromley, C.; Früchtl, H.; Schaub, R. Coupling Epitaxy, Chemical Bonding, and Work Function at the Local Scale in Transition Metal-Supported Graphene. *ACS Nano* **2010**, *4*, 5773–5782.

[18] Corso, M.; Auwärter, W.; Muntwiler, M.; Tamai, A.; Greber, T.; Osterwalder, J. Boron Nitride Nanomesh. *Science* **2004**, *303*, 217-220.

[19] Goriachko, A.; He; Knapp, M.; Over, H.; Corso, M.; Brugger, T.; Berner, S.; Osterwalder, J.; Greber, T. Self-Assembly of a Hexagonal Boron Nitride Nanomesh on Ru(0001). *Langmuir* **2007**, *23*, 2928–2931.

[20] Joshi, S.; Ecija, D.; Koitz,R.; Iannuzzi, M.; Seitsonen, A.P.; Hutter, J.; Sachdev, H.; Vijayaraghavan, S.; Bischoff, F.; Seufert, K.; Barth, J.V.; Auwärter, W. Boron Nitride on Cu(111): An Electronically Corrugated Monolayer. *Nano Lett.* **2012**, *12*, 5821–5828.

[21] Zhang, Q.; Yu, J.; Ebert, P.; Zhang, C.; Pan, C.-R.; Chou, M.-Y.; Shih, C.-K.; Zeng, C.; Yuan, S. Tuning Band Gap and Work Function Modulations in Monolayer hBN/Cu(111) Heterostructures with Moiré Patterns. *ACS Nano* **2018**, *12*, 9355-9362.

[22] zum Hagen, F.H.F; Zimmermann, D.M.; Silva, C.C.; Schlueter, C.; Atodiresei, N.; Jolie, W.; Martínez-Galera, A.J.; Dombrowski, D.; Schröder, U.A.; Will, M.; Lazić, P.; Caciuc, V.; Blügel, S.; Lee, T.-L.; Michely, T.; Busse, C. Structure and Growth of Hexagonal Boron Nitride on Ir(111). *ACS Nano* **2016**, *10*, 11012–11026.

[23] Auwärter, W. Hexagonal Boron Nitride Monolayers on Metal Supports: Versatile Templates for Atoms, Molecules and Nanostructures. *Surf. Sci. Rep.* **2019**, *74*, 1-95.

[24] Zhang, Q.; Chen, Y.; Zhang, C.; Pan, C.-R.; Chou, M.-Y.; Zeng, C.; Shih, C.-K. Bandgap renormalization and work function tuning in $MoSe_2$/hBN/Ru(0001) heterostructures. *Nat. Commun.* **2016**, *7*, 13843.

[25] Zhang, L.; Yang, T.; Sahdan, M.F.; Arramel; Xu, W.; Xing, K.; Feng, Y.P.; Zhang, W.; Wang, Z.; Wee, A.T.S. Precise Layer-Dependent Electronic Structure of MBE-Grown $PtSe_2$. *Adv. Electr. Mater.* **2021**, *7*, 2100559.

[26] Zhang, L.; Yang, T.; Arramel; Feng, Y.P.; Wee, A.T.S.; Wang, Z. MBE-Grown Ultrathin $PtTe_2$ Film and the Layer-Dependent Electronic Structure. *Nanoscale* **2022**, *14*, 7650-7658.

[27] Lasek, K.; Li, J.; Kolekar, S.; Coelho, P.M.; Zhang, M.; Wang, Z.; Batzill, M. Synthesis and Characterization of 2D Transition Metal Dichalcogenides: Recent Progress from a Vacuum Surface Science Perspective. *Surf. Sci. Rep.* **2021**, *76*, 100523.

[28] Villaos, R.A.B.; Crisostomo, C.P.; Huang, Z.-Q.; Huang, S.-M.; Padama, A.A.B.; Albao, M.A.; Lin, H.; Chuang F.-C. Thickness Dependent Electronic Properties of Pt Dichalcogenides. *npj 2D Mater. Appl.* **2019**, *3*, 2.

[29] Lin, M.-K.; Villaos, R.A.B.; Hlevyack, J.A.; Chen, P.; Liu, R.-Y.; Hsu, C.-H.; Avila, J.; Mo, S.-K.; Chuang, F.-C.; Chiang. T.C. Dimensionality-Mediated Semimetal-Semiconductor Transition in Ultrathin $PtTe_2$ Films. *Phys. Rev. Lett.* **2020**, *124*, 036402.

[30] Li, J.; Kolekar, S.; Ghorbani-Asl, M.; Lehnert, T.; Biskupek, J.; Kaiser, U.; Krasheninnikov, A.V.; Batzill, M. Layer-Dependent Band Gaps of Platinum Dichalcogenides. ACS Nano **2021**, *15,* 13249-13259.

[31] Lasek, K.; Ghorbani-Asl, M.; Pathirage, V.; Krasheninnikov, A.V.; Batzill, M. Controlling Stoichiometry in Ultrathin van der Waals Films: $PtTe_2$, Pt_2Te_3, Pt_3Te_4, and Pt_2Te_2. *ACS Nano* **2022**, *16*, 9908–9919.

[32] Yao, W.; Wang, E.; Huang, H.; Deng, K.; Yan, M.; Zhang, K.; Miyamoto, K.; Okuda, T.; Li, L.; Wang, Y.; Gao, H.; Liu, C.; Duan, W.; Zhou, S. Direct Observation of Spin-Layer Locking by Local Rashba Effect in Monolayer Semiconducting $PtSe_2$ Film. *Nat. Commun.* **2017**, *8*, 14216.

[33] Lichtenstein, L.; Heyde, M.; Ulrich, S.; Nilius, N.; Freund, H.-J. Probing the Properties of Metal–Oxide Interfaces: Silica Films on Mo and Ru Supports. *J. Phys.: Condens. Matter* **2012**, *24*, 354010.

[34] Ploigt, H.C.; Brun, C.; Pivetta, M.; Patthey,F.; Schneider, W.-D. Local Work Function Changes Determined by Field Emission Resonances: NaCl/Ag(100). *Phys. Rev. B* **2007**, *76*, 195404.

[35] Ruggiero, C. D.; Choi, T.; Gupta, J.A. Tunneling Spectroscopy of Ultrathin Insulating Films: CuN on Cu(100). *Appl. Phys. Lett.* **2007**, *91*, 253106.

[36] Ruffieux, P.; Aït-Mansour, K.; Bendounan, A.; Fasel, R.; Patthey, L.; Gröning, P.; Gröning, O. Mapping the Electronic Surface Potential of Nanostructured Surfaces. *Phys. Rev. Lett.* **2009**, *102*, 086807.

[37] Zhao, P.; Wan, Y.; Zhang, S.; Gao, A.; Guo, P.; Jiang, Z.; Zheng, J. Strain Effects on the 2D van der Waals Heterostructure C3B/C3N: A Density Functional Theory and a Tight-Binding Study. *Phys. Status Solidi RRL* **2020**, *14*, 2000012.

[38] Joshi, S.; Bischoff, F.; Koitz, R.; Ecija, D.; Seufert, K.; Seitsonen, A.P.; Hutter, J.; Diller, K.; Urgel, J.I.; Sachdev, H.; Barth, J.V.; Auwärter, W. Control of Molecular Organization and Energy Level Alignment by an Electronically Nanopatterned Boron Nitride Template. *ACS Nano* **2014,** *8*, 430-442.

[39] Schulz, F.; Drost, R.; Hämäläinen, S.K.; Liljeroth, P. Templated Self-Assembly and Local Doping of Molecules on Epitaxial Hexagonal Boron Nitride. *ACS Nano* **2013**, *7*, 11121–11128.

[40] Joshi, S.; Bischoff, F.; Koitz, R.; Ecija, D.; Seufert, K.; Seitsonen, A.P.; Hutter, J.; Diller, K.; Urgel, J.I.; Sachdev, H.; Barth, J.V.; Auwärter, W. Control of Molecular Organization and Energy Level Alignment by an Electronically Nanopatterned Boron Nitride Template. *ACS Nano* **2014**, *8*, 430–442.

[41] Urgel, J.I.; Schwarz, M.; Garnica, M.; Stassen, D.; Bonifazi, D.; Ecija, D.; Barth, J.V.; Auwärter, W. Controlling Coordination Reactions and Assembly on a Cu(111) Supported Boron Nitride Monolayer. *J. Amer. Chem. Soc.* **2015,** *137*, 2420-2423.

[42] Widmer, R.; Passerone, D.; Mattle, T.; Sachdev, H.; Gröning, O. Probing the Selectivity of a Nanostructured Surface by Xenon Adsorption. *Nanoscale* **2010**, *2*, 502-508.

[43] Pörtner, M.; Wei, Y.; Riss, A.; Seufert, K.; Garnica, M.; Barth, J.V.; Seitsonen, A.P.; Diekhöner, L.; Auwärter, W. Charge State Control of F_{16}CoPc on h -BN/Cu(111). *Adv. Mater. Interf.* **2020,** *7*, 2000080.

[44] Liu, L.; Dienel, T.; Widmer, R.; Gröning, O. Interplay Between Energy-Level Position and Charging Effect of Manganese Phthalocyanines on an Atomically Thin Insulator. *ACS Nano* **2015**, *9*, 10125–10132.

[45] Chia, X.; Adriano, A.; Lazar, P.; Sofer, Z.; Luxa, J.; Pumera, M. Layered Platinum Dichalcogenides (PtS_2, $PtSe_2$, and $PtTe_2$) Electrocatalysis: Monotonic Dependence on the Chalcogen Size. *Adv. Funct. Mater.* **2016**, *26*, 4306-4318.

[46] Rosli, N.F.; Mayorga-Martinez, C.C.; Latiff, N.M.; Rohaizad, N.; Sofer, Z.; Fisher, A.C.; Pumera, M. Layered $PtTe_2$ Matches Electrocatalytic Performance of Pt/C for Oxygen Reduction Reaction with Significantly Lower Toxicity. *ACS Sustain. Chem. Eng.* **2018**, *6*, 7432−7441.

[47] Huang, H.; Fan, X.; Singh, D.J.; Zheng, W. Modulation of Hydrogen Evolution Catalytic Activity of Basal Plane in Monolayer Platinum and Palladium Dichalcogenides. *ACS Omega* **2018**, *3*, 10058−10065.

[48] Clark, O.J.; Mazzola, F.; Feng, J.; Sunko, V.; Markovic, I.; Bawden, L.; Kim, T.K.; King, P.D.C.; Bahramy, M.S. Dual Quantum Confinement and Anisotropic Spin Splitting in the Multivalley Semimetal $PtSe_2$. *Phys. Rev. B* **2019**, *99*, 045438.

[49] Avsar, A.; Ciarrocchi, A.; Pizzochero, M.; Unuchek, D.; Yazyev, O.V.; Kis, A. Defect Induced, Layer-Modulated Magnetism in Ultrathin Metallic $PtSe_2$. *Nat. Nanotechnol.* **2019**, 14, 674–678.

[50] Avsar, A.; Cheon, C.-Y.; Pizzochero, M.; Tripathi, M.; Ciarrocchi, A.; Yazyev, O.Y.; Kis, A. Probing Magnetism in Atomically Thin Semiconducting $PtSe_2$. *Nat. Commun.* **2020**, *11*, 4806.

[51] Lasek, K.; Li, J.; Ghorbani-Asl, M.; Khatun, S.; Alanwoko, O.; Pathirage, V.; Krasheninnikov, A.V.; Batzill, M. Formation of In-Plane Semiconductor–Metal Contacts in 2D Platinum Telluride by Converting $PtTe_2$ to Pt_2Te_2. *Nano Lett.* **2022**, *22*, 9571–9577.

[52] Kresse, G.; Furthmüller, J. Efficiency of Ab-Initio Total Energy Calculations for Metals and Semiconductors Using a Plane-Wave Basis Set. *Comp. Mat. Sci.* **1996**, 6, 15-50.

[53] Kresse, G.; Furthmüller, J. Efficient Iterative Schemes for Ab Initio Total-Energy Calculations Using a Plane-Wave Basis Set. *Phys. Rev. B* **1996**, 54, 11169-11186.

[54] Perdew, J.P.; Burke, K.; Ernzerhof, M. Generalized Gradient Approximation Made Simple. *Phys. Rev. Lett.* **1996**, 77, 3865-3868.

[55] Tawfik, S. A.; Gould, T.; Stampfl, C.; Ford, M. J. Evaluation of van der Waals Density Functionals for Layered Materials. *Phys. Rev. Mater.* **2018**, 2, 034005.

[56] Momma, K.; Izumi, F. VESTA: A Three-Dimensional Visualization System for Electronic and Structural Analysis. *J. Appl. Cryst.* **2008**, 41, 653-658.